ELSEVIER

NeuroImage

www.elsevier.com/locate/ynimg
NeuroImage 41 (2008) 1278–1292

Detection of focal changes in human cortical thickness: Spherical wavelets *versus* Gaussian smoothing

Jorge L. Bernal-Rusiel,[a,b] Mercedes Atienza,[a] and Jose L. Cantero[a,*]

[a]*Laboratory of Functional Neuroscience, University Pablo de Olavide, Seville, Spain*
[b]*Medical Biophysics Center, University of Oriente, Santiago de Cuba, Cuba*

Received 17 July 2007; revised 14 February 2008; accepted 17 March 2008
Available online 26 March 2008

Subtle but progressive variations in human cortical thickness have been associated with the initial phases of prevalent neurological and psychiatric conditions. But slight changes in cortical thickness at preclinical stages are typically masked by effects of the Gaussian kernel smoothing on the cortical surface shape descriptors. Here we present the first study aimed at detecting changes in human cortical thickness maps by applying soft-thresholding to multiresolution spherical wavelet coefficients. In order to make Gaussian and wavelet smoothing methods comparable, the trade-off between sensitivity and specificity was optimized to detect simulated thickness changes in various cortical areas of healthy elderly subjects. Results revealed a better sensitivity–specificity trade-off when using wavelet-based methods as compared to Gaussian smoothing in both the whole neocortex ($p<10^{-7}$) and cortical region-based statistical analyses ($p<10^{-9}$), which was mainly due to the higher specificity obtained with the wavelet approach. The lower smoothing introduced by wavelets and their adaptive properties may account for the enhanced specificity and sensitivity when compared with Gaussian spatial filters. These results strongly support the use of spherical wavelet methods to detect subtle variations in cortical thickness maps, which may be crucial in better understanding the course of neuronal loss in normal aging and in finding early markers of cortical degeneration.

Keywords: Cortical thickness; Spherical wavelets; Gaussian smoothing; Cortical atrophy; Aging; Neurodegenerative diseases

Introduction

The anatomical integrity of cortical networks distributed within and across different cortical structures leads to integration and segregation patterns of neural activity at various spatiotemporal scales, which have been postulated as potential mechanisms underlying the emergence of higher cognitive functions and motor acts (Uhlhaas and Singer, 2006). Focal but progressive neuronal death causes irreversible changes in functional organization of the human neocortex which may explain slight cognitive impairments associated with age or with different pathological conditions. Therefore, the identification of subtle morphological changes using non invasive *in vivo* techniques is critical to link mild cognitive decline with the preclinical stages of several neurological diseases characterized by cortical neurodegeneration.

Geometrically, the cerebral cortex is a thin, folded sheet of grey matter with a considerable variability in size, location, and extent of the sulci and gyri in humans (Amunts et al., 2002). Modern imaging technologies in combination with remarkable developments in computational neuroanatomy techniques have made possible the *in vivo* detection and quantification of changes in the neocortex (Duncan et al., 2004; Good et al., 2001; Thompson et al., 2004, 2007). Among descriptors, differences in cortical thickness seem to be one of the most reliable markers of structural changes in cortical morphology, which is mainly supported by the fact that excessive cortical expansion is not accompanied by comparable increases in cortical thickness during development or throughout evolution (Rakic, 1988).

Furthermore, there is growing evidence that regional disease-related patterns of cortical thickness not only are associated with cognitive deterioration in normal aging (Fjell et al., 2006), but also in neurological and psychiatric populations (Makris et al., 2007; Butman and Floeter, 2007; Biega et al., 2006; Lyoo et al., 2006; Preul et al., 2005). For instance, Singh et al. (2006) reported cortical thinning of different brain structures involving the frontal, parietal and medial temporal lobes in patients with mild cognitive impairment as compared to controls. In patients who later converted to Alzheimer's disease, a thinning of the entire cortex with significant extension into the lateral temporal lobe was quantitatively determined (Thompson et al., 2001; Lerch et al., 2005; Singh et al., 2006). This specific pattern of changes in cortical thickness characterizing early stages of Alzheimer's disease differs from the

* Corresponding author. Laboratory of Functional Neuroscience, University Pablo de Olavide, Ctra. de Utrera, Km. 1, 41013-Seville, Spain. Fax: +34 954 349151.
E-mail address: jlcanlor@upo.es (J.L. Cantero).
Available online on ScienceDirect (www.sciencedirect.com).

1053-8119/$ - see front matter © 2008 Elsevier Inc. All rights reserved.
doi:10.1016/j.neuroimage.2008.03.022

one found in multiple sclerosis, where cortical thinning was especially evident in the anterior cingulate cortex, the insula and transverse temporal gyrus, and areas of association cortex (Charil et al., 2007; Sailer et al., 2003). The selective thinning within the temporal and prefrontal cortices observed in schizophrenia patients has been further attributed to the neuropsychological deficits of this psychiatric disorder in a variety of cognitive domains (Kuperberg et al., 2003). Patients with bipolar disorder have also shown decreased thickness in different structures of prefrontal cortex (orbitofrontal, dorsolateral and cingulate regions), supporting both the disruption hypothesis of prefrontal and anterior cingulate cortex, and the uncontrolled emotions characteristic of this type of depressive illness (Lyoo et al., 2006). On the other hand, Shaw et al. (2006) recently established a longitudinal pattern of prefrontal cortex thinning, comprising critical regions associated with attentional networks, which may be useful in characterizing and/or predicting clinical outcome in children suffering from attention-deficit/hyperactivity disorders.

Statistical testing of changes in cortical thickness maps obtained with computational neuroanatomy methods requires spatial smoothness of the data. Spatial smoothing has the ability to i) increase the signal to noise ratio by removing the high-frequency noise from cortical thickness measures, and to ii) enhance the validity of parametric statistical tests by reducing between-subject differences and the effective number of comparisons in the cortical surface. Unfortunately, spatial smoothing can also result in a noticeable decrease in specificity. The width of the Gaussian kernel is an important parameter in determining the trade-off between precision and reliability of the smoothed thickness maps. Thus, narrower kernels will leave unnecessary noise in the data, whereas wider kernels will blur the exact location of the cortical change (Hagler et al., 2006). The output result of the Gaussian blurring may severely reduce the submillimeter precision of thickness measurements as well as the necessary level of accuracy to localize small cortical atrophies associated with neurological and psychiatric dysfunction.

In the last few years, a growing number of studies have tested statistical parametric maps in the wavelet domain (Bullmore et al., 2003). The multiresolution representation of data provided by the wavelet transform seems well suited to feature detection problems, especially if the size of the feature is unknown *a priori* (Nenadic and Burdick, 2005; Daubechies and Teschke, 2005; Antoine et al., 2002). Among other advantages, the wavelet transform preserves spatial edges better than, for example, the Fourier transform. These edges are typically raised on the images due to sharp transitions between small and relatively high voxel values. These salient features are better codified by wavelet transforms because they control the extent of both frequency and spatial scales, unlike the infinite spatial extent of the cosines and sines of the Fourier transform. For example, a wavelet transform well spatially localized near the edges is able to capture the high-frequency changes while retaining much less information on those uniform parts of the image that mainly contain low-frequency components. Therefore, given an appropriate basis, the wavelet transform approximately concentrates the power into a smaller number of coefficients, which makes it especially attractive to reduce complex images to their most relevant features (Mallat, 1999; Daubechies, 1992). In summary, wavelet transforms adapt surface changes at different scales and spatial locations (Kavitha and Ramakrishnan, 2005; Laine, 2000; Cesar and Costa, 1998), overcoming the above-mentioned drawbacks derived from the traditional monoresolution Gaussian filters. Wavelet-based smoothing approaches have been previously used in context of functional magnetic resonance imaging (fMRI) studies, resulting in a general increase of sensitivity and specificity after controlling the proportion of false positives that stem from the multiple comparison tests (Van de Ville et al., 2006; Fadili and Bullmore, 2004; Wink and Roerdink, 2004).

Given that human cortical hemispheres can be modeled as a convoluted surface with spherical topology, the cortical surface can be mapped onto a parameterized sphere to establish a spherical coordinate system (Fischl et al., 1999a; Van Essen et al., 1998). Multiscale shape representations of cortical surfaces have recently been introduced by applying spherical wavelets. Results from these studies suggest that spherical wavelets improve the approximation of cerebral surfaces by capturing finer shape details within different cortical and subcortical structures (Yu et al., 2007; Nain et al., 2007). But no studies have systematically evaluated variations in cortical thickness using spherical wavelets. Wavelet-based smoothing methods are expected to enhance the trade-off between sensitivity and specificity when compared with the Gaussian kernel filter typically used to smooth statistical parametric maps.

Here we present the first study aimed at detecting changes in cortical thickness maps by applying spherical wavelets to the description of the human neocortex. Obtained results were compared with Gaussian kernel smoothing in a series of thickness statistical parametric maps using the false discovery rate (FDR) as an alternative solution to the problem of multiple comparisons. The performance of the two smoothing methods was evaluated by simulating different levels of thinning in various cortical areas of healthy elderly subjects.

Materials and methods

Subjects

A total of 70 non-demented subjects (aged 60–96 yr, 53 women) extracted from the OASIS database were selected for the present study. Inclusion criteria consisted of Mini-Mental State Examination (MMSE) of $\geq$29 (high level of functioning), and Clinical Dementia Ratings (CDR) of 0 (no dementia). Participants were split into two groups of 35 subjects (control and experimental). Gender and age were balanced between these two groups (Control: 75$\pm$8.04 yr; Experimental: 75$\pm$9.77 yr).

Image acquisition

Four high-resolution structural T1-weighted magnetization-prepared rapid gradient echo (MP-RAGE) images were acquired in the same session on a 1.5-T Vision™ scanner (Siemens, Erlangen, Germany). MP-RAGE parameters were empirically optimized for grey/white contrast (repetition time=9.7 ms, echo time=4 ms, flip angle=10°, inversion time=20 ms, delay time=200 ms, 256$\times$256 [1 mm$\times$1 mm] in-plane resolution, 128 sagittal 1.25 mm slices without gaps, time per acquisition=6.6 min).

Thickness map computation

For each subject, the four MP-RAGE volumes were averaged after motion correction to generate a single volume with a better signal to noise ratio. Construction of the cortical surface was performed with the Freesurfer software that provides a set of tools for analysis and visualization of brain imaging data (http://surfer.nmr.mgh.harvard.edu/). Non uniformity correction (intensity normalization) and skull

stripping algorithms were applied to the images prior to white matter segmentation. Segmentation was further refined and cut to generate a single connected mass of each cerebral hemisphere. The surface of the labeled white matter of each hemisphere was then tessellated with a triangular mesh to obtain the grey/white surface. This surface was first deformed outwards to the location in the volume with highest intensity contrast between the grey matter and the cerebrospinal fluid and, later, it was refined to generate the pial surface. White matter-based deformation methods have provided accurate representations of the cortical shape without requiring additional measures to force the surface into the depth of the cerebral sulci (Dale et al., 1999).

Given the non Euclidian intrinsic geometry of cortical surfaces, spherical mapping of cortical thickness maps was used to bring the cortical thickness manifold onto a spherical coordinate system for which a suitable parameterization, surface registration and basis were previously provided (Fischl et al., 1999a; Van Essen et al., 1998). Cortical surfaces were constrained to have a spherical topology by applying an automatic topology correction algorithm. This algorithm first transformed the inflated surface to a parametric surface with spherical coordinates, then corrected its topology, and finally performed the backward transforms (Fischl et al., 2001). The surfaces mapped onto a sphere with minimal metric distortion were registered to the spherical coordinate system with a spherical template by non-linearly aligning each individual cortical folding pattern with the average folding pattern (Fischl et al., 1999b). This procedure ensures that every vertex on the individual surface has a unique coordinate that belongs to the same anatomofunctional cortical area on the average surface.

Once highly accurate models of both grey/white and pial surfaces were obtained, the cortical thickness map was generated as follows: For each point on the grey/white surface, the shortest distance to the pial surface was first computed. Next, for each point on the pial surface, the shortest distance to the grey/white surface was calculated. The thickness at each vertex was set at the average of these two values (Fischl and Dale, 2000). Thickness values were then calculated in the native brains rather than in the Talairach space to increase the power of statistical tests (Ad-Dab'bagh et al., 2005). Only left hemisphere cortical thickness maps were considered in the present study. In order to obtain the thickness map of each subject on the same coordinate system, every thickness map was resampled to a standard template surface (Desikan et al., 2006) using the non-linear spherical registration algorithm (Fischl et al., 1999b). After resampling, all the thickness maps showed an identical number of vertices, and each vertex had the same spherical coordinates across subjects. Fig. 1 summarizes the processing steps followed in the present study.

Simulated changes in cortical thickness

In order to determine differences in sensitivity and specificity between the Gaussian smoothing and spherical wavelets at detecting cortical atrophies, a range of variable thinning was artificially introduced into different cortical regions of the experimental group ($N=35$). Importantly, the anatomical regions chosen for the present simulation study were shown to decrease in thickness from normal aging to mild cognitive impairment, as well as in the progression to Alzheimer's disease (Singh et al., 2006). Thus, synthetic thinning was introduced in four cortical regions: entorhinal cortex (Brodmann's area 28), medial orbitofrontal cortex (Brodmann's area 11), inferior temporal lobe (Brodmann's area 20) and the medial part of the temporal lobe (Brodmann's area 21). Cortical parcellation was computed by subdividing the human cerebral cortex into standard

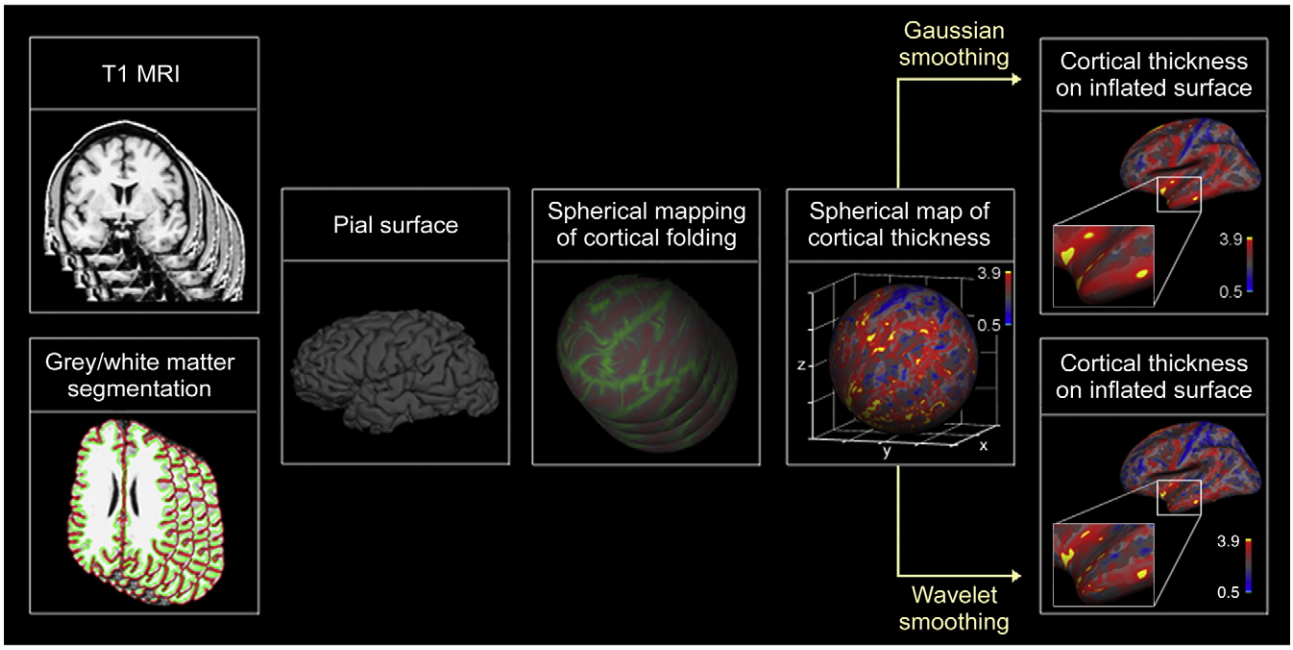

Fig. 1. Flow chart showing the main image processing steps used in the present study. Extraction of cortical surface was performed automatically on the T1-MRI scans of 70 healthy elderly subjects (synthetic changes in cortical thickness were introduced in 35 of them). Cortical folding patterns were registered in the spherical coordinate system by aligning each individual cortical folding pattern with the average folding pattern, allowing mapping and smoothing of the cortical thickness pattern on the sphere with different smoothing approaches (Gaussian *versus* spherical wavelets). Values of the colormap bars introduced in the last two columns are expressed in mm.

gyral-based neuroanatomical regions (Desikan et al., 2006). For each of these areas, we randomly selected five regions of interest (ROIs) with different sizes (at about 20, 30, 40, 50, and 60 cm^2) in the spherical surface template. This template is represented by a seven order icosahedron with a total surface of 12,565 cm^2 (163,842 vertices). Each ROI size was determined by adding the area of all triangle faces within the same ROI. The area of each triangle was computed with the Heron's formula by using the spherical coordinates of its vertices. However, a fixed area on the template surface does not guarantee a fixed number of vertices. Although the same number of triangles was used to generate the different ROIs, the number of shared vertices depended on the spatial distribution of such triangles. Thus, the total number of vertices is not only determined by the area size but also by the shape of the modified area. Table 1 shows the four selected ROIs and the corresponding number of vertices affected by the subsequent thickness reduction.

A statistical collateral effect of introducing the same thinning percent within a ROI across different subjects is the significant decrease of the intersubject variability inside that specific ROI. Consequently, small Gaussian kernels always will provide a better sensitivity–specificity trade-off than larger kernels. In order to illustrate the classical increase of the trade-off up to a point from which it decreases again, intersubject variability was artificially increased for each vertex inside the whole Brodmann's areas mentioned above after resampling the individual surfaces to the spherical template surface. For the experimental group, mean cortical thickness was artificially decreased by 5% to 15%. To get this overall percent of change, a certain percent of change (p_8) was introduced at the same vertex of eight randomly selected subjects for every vertex within each Brodmann's area by applying the following formula:

$$p_8 \approx \frac{35}{8} p_{35}$$

where p_{35} represents the overall percent of thinning. For example, introducing an overall 10% of cortical thinning at one particular vertex of the experimental group would require that cortical thickness at that vertex be reduced by 43.7% in any eight of the thirty-five experimental subjects.

Synthetic changes in cortical thickness were then obtained by further reducing the thickness values within the ROIs across the 35 experimental subjects. From every noisy thickness map, 5 new maps were obtained by artificially reducing the thickness values of each ROI by 5%, 10%, 15%, 20%, and 25% for every subject. The mean thickness reduction (in mm) modified for each ROI size is shown in Table 2.

The twenty-five maps resulting from combining the five thickness reductions and the five ROIs selected for every subject (N=35) were compared with the maps generated for the control group (N=35) which included no synthetic changes either in cortical thickness or intersubject variability.

Table 1
ROI size and number of vertices modified within each ROI

Change size (cm^2)	ROIs			
	Inferior temporal	Medial temporal	Entorhinal	Medial orbitofrontal
20	205	227	228	225
30	318	262	266	261
40	414	353	403	308
50	468	327	393	441
60	474	588	482	459

Table 2
Mean cortical thinning (mm) across subjects over all the vertices in each of the ROIs in different cortical regions

Cortical regions	Percent of thickness reduction				
	ROI size	5%	10%	15%	20%	25%
Inferior temporal						
	20 (cm^2)	0.46	0.60	0.81	1.82	1.04
	30 (cm^2)	0.47	0.49	0.68	0.77	0.88
	40 (cm^2)	0.39	0.43	0.57	0.68	0.74
	50 (cm^2)	0.49	0.66	0.72	0.79	1.02
	60 (cm^2)	0.41	0.54	0.63	0.76	0.81
Medial temporal						
	20 (cm^2)	0.63	0.59	0.80	0.93	1.08
	30 (cm^2)	0.53	0.60	0.80	0.88	0.98
	40 (cm^2)	0.52	0.68	0.79	0.92	0.97
	50 (cm^2)	0.49	0.64	0.76	0.83	0.95
	60 (cm^2)	0.49	0.53	0.7	0.88	1.01
Entorhinal						
	20 (cm^2)	0.44	0.61	0.64	0.74	0.91
	30 (cm^2)	0.51	0.57	0.67	0.90	0.97
	40 (cm^2)	0.60	0.61	0.72	0.86	1.01
	50 (cm^2)	0.51	0.62	0.78	0.85	0.97
	60 (cm^2)	0.52	0.68	0.77	0.89	0.95
Medial orbitofrontal						
	20 (cm^2)	0.30	0.41	0.43	0.47	0.56
	30 (cm^2)	0.35	0.41	0.49	0.55	0.60
	40 (cm^2)	0.33	0.42	0.46	0.56	0.67
	50 (cm^2)	0.32	0.44	0.48	0.58	0.66
	60 (cm^2)	0.37	0.43	0.51	0.62	0.64

Application of Gaussian kernel smoothing to cortical thickness maps

The Gaussian smoothing operator has been classically used to remove unnecessary details and high-frequency noise from biomedical images (e.g., Hagler et al., 2006; Petersson et al., 1999). The Gaussian kernel smoothing of the signal $f(x)$ in n-dimension with full width at half maximum (FWHM)=$4(\ln 2)^{1/2}t$ is defined as the convolution of the n-dimensional Gaussian kernel $G(x,t)$ with signal $f(x)$, i.e. $F(x,t)=f*G(x;t)$. The convoluted signal F is the solution of a diffusion equation $\partial F/\partial t = L[F]$ with the initial condition $F(x,0)=f(x)$ and the n-dimensional Euclidean Laplacian L. The generalization of the Laplace operator L to an arbitrary Riemannian curved surface is called the Laplace–Beltrami operator, and the resulting surface Gaussian kernel smoothing is known as diffusion smoothing (Chung et al., 2003). This generalization takes into account the geodesic surface and acts as a low-pass isotropic spatial frequency filter on the manifold. As a result, the resolution and sensitivity provided by the diffusion smoothing is higher as compared with the 3D volumetric smoothing.

The implementation of Gaussian smoothing filters in Freesurfer is based on the iterative nearest-neighbor averaging procedure which simulates the solution of the linear diffusion equation on the surface mesh. In this procedure, the width of the kernel determines the total number of iterations (Han et al., 2006).

There is evidence that variability declines and sensitivity improves with increasing FWHM up to a point, after which both variability and sensitivity decline again (Lerch and Evans, 2005). In the present simulation study the FWHM of the surface smoothing kernel was varied for the whole brain (global-based statistical analyses) and for each cortical region (local-based statistical analyses) in order to select the ones which showed an optimal trade-off between sensitivity and the consequent lost in specificity across the estimated statistical parametric maps.

Application of wavelet soft-thresholding algorithms to spherical cortical thickness maps

The wavelet transform provides local information about the spatial scales of an image (Laine, 2000). The salient information is compressed in a few wavelet coefficients which represent the most relevant image features. This compression is crucial in wavelet-based denoising schemes because white noise is distributed over the whole set of coefficients. Consequently, the wavelet transform may be used to produce smoothed estimations of a map (Mallat, 1989). Classical constructions have been restricted to simple domains such as intervals and rectangles. However, wavelet constructions for scalar functions can also be defined on the sphere (Antoine et al., 2001; Wiaux et al., 2005), enabling the wavelet-based analysis of spherical data. Therefore, spherical wavelets are completely defined on the sphere and obtained by translation (rotation) and scaling of a mother wavelet.

Spherical wavelets were discretized on equiangular spherical grids. These grids have been used to build the Spherical Harmonic Transform (SHT) on the 2-sphere(S^2) (Driscoll and Healy, 1994), which later served to construct the Spherical Continuous Wavelet transform (Antoine et al., 2001; Wiaux et al., 2005). Equiangular grids are defined as:

$$\wp_i = \left\{(\theta_{\mathrm{im}},\varphi_{\mathrm{in}})\in S^2 : \theta_{\mathrm{im}} = \frac{(2m+1)\pi}{4B_i}, \varphi_{\mathrm{in}} = \frac{n\pi}{B_i}\right\}; m,n\in \mathrm{T_i} \equiv \{k\in N: k<2B_i\},$$

the bandwidth being $\{B_i\in 2N, i\in Z\}$. Any function $f\in L^2(S^2)$ of bandwidth B_i can be sampled without loss of information on this grid.

Spherical cortical thickness maps of the left-brain hemisphere were resampled from the icosahedron to equiangular grids using standard nearest-neighbor interpolation based on Delaunay triangulations (Watson, 1992). As both the number of rows and columns for the equiangular grids must be a power of two, grids of $1024\theta\times 1024\varphi$ and $2048\theta\times 2048\varphi$ were used because they constitute the best trade-off between grid resolution and computational time for the transformations.

Cortical thickness maps in both control and experimental subjects were filtered by using a pyramidal decomposition based on axis-symmetric Spherical Discrete Wavelet Frames (SDWF) (Wiaux et al., 2007). This analysis represents an evolution of the wavelet formalism developed by Antoine and Vandergheynst (1999) and Wiaux et al. (2005). In this new transformation, a dyadic discretization is adopted for the scales of dilation in harmonic space on S^2. Unlike previous definitions of dilations in harmonic space (McEwen et al., 2006), the new formalism provides control on evolution of the filter localization properties in real space (Wiaux et al., 2007).

Spherical Convolution (SC) of two functions living on S^2 is defined as the point wise product between the Spherical Harmonic Coefficients (SHCs) of one function and the SHCs of the other. The SDWF transformation for a signal with bandwidth B and with filters sampled on the corresponding grid in the harmonic space follows the steps below:

i) *Wavelet coefficient generation in harmonic space*. At the first decomposition level, the detail (high-frequency) and approximation (low-frequency) wavelet coefficients are obtained after performing the SC of the original signal and the corresponding high- and low-pass filters, respectively. For the approximation coefficients, only the SHCs corresponding to frequencies lower than *B/2* are maintained. The filters are downsampled at each j decomposition level by taking only their odd samples. Then, the SC of the approximation coefficients at level $j-1$ and the downsampled high- and low-pass filters provide the detail and approximation coefficients at level j, respectively. For the latter, only the SHCs that correspond to frequencies lower than $B/2^j$ are preserved.

ii) *Transformation of wavelet coefficients into real space*. The inverse SHT of both approximation coefficients at the last decomposition level and detail coefficients at all decomposition levels is computed to transform them into real space. This transformation is possible because the wavelet coefficients also live on S^2 for spherical axis-symmetric filters (as opposed to axis-asymmetric filters).

iii) *Signal reconstruction from wavelet coefficients in harmonic space* proceeds through the same operations as decomposition, but in reverse order. In other words, the reconstruction is achieved by recursively doubling the frequency resolution of the approximation wavelet coefficients in harmonic space (padding the higher frequencies with zeros) and computing SC with the corresponding up sampled versions of the low-pass filter. This procedure generates the low-frequency components of the signal at each decomposition level. Additionally, SC of the detail wavelet coefficients and the corresponding up sampled high-pass filter are computed to generate the high-frequency components. Both components are added at each step to generate an approximation signal in harmonic space at each level.

iv) *Transformation of the approximation signal into real space*. The inverse SHT of the approximation signal at the last step is computed to get the signal into real space. The original signal can be recovered when wavelet coefficients are not modified.

Similar invertible filter banks have been proposed in Yeo et al. (2006), but they used stereographic dilation directly in real space. Nevertheless, this kind of dilation makes it difficult to control the localization properties of wavelets (and wavelet coefficients) in harmonic space because the effect on the SHCs of the dilated function is not analytical.

In particular, the scale discretized axis-symmetric filters employed in the present study are related in harmonic space by equations:

$$H^2 = \frac{\phi^2(l)}{\phi^2\left(2^{-1}l\right)} \quad (\mathrm{low-pass\ filter})$$

$$G^2 = 1 - H^2 \quad (\mathrm{high-pass\ filter})$$

where ϕ is a scale discretized scaling function of a positive real variable l and is given in harmonic space by:

$$\phi^2(l) = \mathrm{e}^{-l^2} \sum_{k=0}^{p-1} \frac{l^{2k}}{k!}.$$

The variable l represents the overall frequencies on the sphere (Wiaux et al., 2007) whereas the value of the oscillation factor P controls the shape of the filters. Scale discretized scaling function can be obtained from a continuous wavelet provided that it fulfils the specific conditions established in Wiaux et al. (2007).

To get a smoothed approximation of the signal, we used a non-linear denoising technique based on translation of multiresolution spherical wavelet coefficients towards zero by applying a threshold value (soft-thresholding) (Donoho, 1995). Soft-thresholding provides considerable noise reduction without greatly impairing the spatial resolution of the denoised function.

The maximum allowed decomposition levels were introduced in the SDWF transformation, 7 for the grids of $1024\theta \times 1024\varphi$ and 8 for the grids of $2048\theta \times 2048\varphi$.

The first decomposition level contained the real space wavelet coefficients of the finest scale and were the same size as the original signal. The number of columns and rows of the grids are reduced by half across subsequent levels until 8×8 at the last coarsest level, which contain the approximation wavelet coefficients. Further reduction of the grids is not allowed by the SHT implementation (Healy et al., 2003) because it requires bandwidth greater than or equal to 4 for transformation of the signal.

The denoising procedure based on wavelet soft-thresholding not only smoothes but also preserves quite well the shape of the signal. Indeed, the reconstructed function is at least as smooth as the estimated one; and the estimator comes nearly as close in mean square to the estimated function as any measurable estimator can come, over every one of a wide range of smoothness classes. These two properties, mathematically proven by Donoho (1995), make the denoising procedure quite suitable for our purposes.

The value of the threshold for the soft-thresholding procedure was obtained by reshaping the matrix of the wavelet coefficients at the finest scale on a one-dimensional vector c. After that, the threshold value was computed as follows:

$$\mathrm{thr} = \frac{\mathrm{median}(\mathrm{abs}(c))\sqrt{2 \ \log \ (n)}}{0.6745}$$

where n represents the length of vector c. In our case, n was equal to 1024^2 for the grids of $1024\theta \times 1024\varphi$ and 2048^2 for the $2048\theta \times 2048\varphi$ grids. Donoho and Johnstone (1994) demonstrated that these universal thresholds have a robust noise level estimator in the wavelet space. Additionally, they have also reported that the wavelet-based signal estimator has a minimax error asymptotically close to that of the optimal unknown thresholding rule.

Like the Gaussian smoothing, an optimal filter was obtained for the whole brain (global-based statistical analyses) and for each cortical region (local-based statistical analyses) by varying three parameters of the filtering process with wavelets. These parameters include i) the oscillation factor which controls the shape of the filters; ii) the dilation factor which scales the initial support (dilation) of the filters in harmonic space (and therefore in the real space); and iii) the number of the finest decomposition levels at which the thresholding procedure is applied.

Determining optimal Gaussian and wavelet filters

There is a classical trade-off between enhancing sensitivity by increasing smoothness of the statistical parametric maps and the consequent loss in specificity and image resolution (Lerch et al., 2005; Han et al., 2006; Singh et al., 2006). We followed the standard definitions of sensitivity [#true positives/(#true positives+#false negatives)] and specificity [#true negatives/(#true negatives+#false positives)], while the optimal Gaussian and wavelet filters were operationally defined as those ensuing from the best trade-off between sensitivity and specificity across the 25 statistical parametric maps resulting from the simulation study. This trade-off was estimated with the equation $t = \mathrm{mean}(\mathrm{sensitivity}_i * \mathrm{specificity}_i)$, where $i = 1 \ldots 25$. Optimal filters were first established for the global-based statistical analyses considering the whole cerebral cortex and, then, for local-based statistical analyses considering each of the four cortical regions separately.

Measuring the intersubject variability in cortical thickness

One of the principal aims of biomedical image smoothing is to reduce the intersubject variability for subsequent statistical analyses. Indeed, Han et al. (2006) found that variability in cortical thickness measurements became smaller as the kernel size of the Gaussian filter increased (see also Chung et al., 2005). We compared the intersubject variability yielded by the two methods (Gaussian smoothing *versus* spherical wavelets) in order to determine whether this error source might partially explain differences at detecting variations in cortical thickness. For the global effects, intersubject variability was obtained by averaging the standard deviations in all vertices of the cortical thickness maps (left hemisphere) from control and experimental groups separately, after they were resampled on the template surface. Since variability is not uniform across the cortex (Lerch and Evans, 2005), we further computed the intersubject variability for those four specific cortical regions where the simulated ROIs were introduced (local effects).

Statistical analysis

Generation of thickness statistical parametric maps was accomplished by means of a mass vertex-based analysis using the univariate general linear model at each cortical vertex. The goal was to test for the null hypothesis of no group differences on the cortical thickness at each cortical vertex. The value of the Fisher's F statistic was used for this purpose. Multiple comparisons were corrected using the false discovery rate (FDR) correction (Genovese et al., 2002) at 0.01 level of significance. This correction procedure ensured that, on the average, only 1% of the surviving results were statistically false positives, whereas those remaining stemmed from the spatial smoothing process. An FDR threshold was then determined from the observed p-value distribution. There is evidence that FDR is independent of hypothesis testing and the smoothing method (Wink and Roerdink, 2004). Comparisons between different smoothing methods were then possible using the same FDR. This procedure is extremely simple to implement and has been previously employed in exploratory studies using cortical thickness analysis (Singh et al., 2006; Lerch et al., 2005; Lerch and Evans, 2005).

Sensitivity, specificity and the trade-off between these two measurements provided by the optimal filters after applying global FDR thresholding to thickness statistical parametric maps were evaluated with one-way analyses of variance (ANOVAs) with

repeated measures. These models only included the smoothing method (Gaussian, wavelet transform on grids of 1024^2, wavelet transform on grids of 2048^2) as the within-subject factor. In the case of the local FDR thresholding, a two-way ANOVA was applied to the cortical region (inferior temporal lobe, medial temporal lobe, entorhinal cortex and medial orbitofrontal cortex) included as an additional within-subject factor. Mauchly's *W* was computed to check for violations of the sphericity assumption. When Mauchly's *W* test was significant, the Greenhouse–Geisser correction was applied (and the epsilon index was reported). Homogeneity of variance was evaluated with the Levene's test. The Tukey test was performed for post-hoc comparisons.

Finally, the number of subjects per group required in order to detect significant changes in cortical thickness maps smoothed with the wavelet-based procedure at the optimal setting was determined by a power analysis.

Results

Optimal smoothing filters for the Gaussian and wavelet approximation

As shown in Fig. 2A, increasing the kernel size improved the trade-off between sensitivity and specificity up to a point. The best trade-off was found at 14 mm FWHM for the whole cerebral cortex. The optimal kernel size decreased when the FDR threshold was locally computed for each cortical region separately (Fig. 2B). For the middle and inferior regions of the temporal lobe as well as for the medial orbitofrontal cortex, the optimal kernel size was 2 mm while for the entorhinal cortex the trade-off increased up to a blurring kernel of 10 mm.

In the case of the wavelet-based method, three different parameters were manipulated: the oscillation and dilation factors, and the number of the finest decomposition levels at which the thresholding procedure was applied. The best results were always obtained with an oscillation factor of 1. In this particular case, the low-pass filter becomes Gaussian whereas the wavelet associated with the high-pass filter becomes a difference of Gaussians. The other two parameters varied depending on the smoothing required to get an optimal wavelet filter able to compete with the optimal empirically determined Gaussian kernel. Thus, for narrow Gaussian kernels the optimal wavelet filters showed smaller dilation factors and fewer numbers of threshold-finest decomposition levels as compared to relatively wide kernels. In addition, increasing the resolution of the equiangular grid from 1024^2 to 2048^2 samples resulted in improved results. This grid shift also increased the dilation factor required for the corresponding optimal filter. Indeed, the dilation factors for the best global wavelet filters were 6 and 11 for the grids of 1024^2 and 2048^2 samples, respectively. For the local analyses, the optimal dilation factors varied from 4 to 5 except for the entorhinal cortex which increased from 5 to 7 for the grids of 1024^2 and 2048^2 samples, respectively. The number of threshold-finest levels was set to 3 at the global level and also at the local level, in particular for the entorhinal cortex, but it was reduced to 1 for the remaining regions.

Gaussian spatial filter versus wavelet-based smoothing: computational times and qualitative evaluation

Both smoothing approaches to cortical thickness maps were computed in Dell™ workstations with 4 Intel Xeon™ Dual Core processors, 2.66 GHz each, 16.0 GB of RAM, using MATLAB® v. 7.3 under Linux Centos4 X86-64 bits. Application of the spherical wavelet-based smoothing method per subject took about 37 s for grids of 1024^2 and about 4.1 min for grids of 2048^2. This time included the resampling of the icosahedron thickness surface to the equiangular grid, computation of the SDWF transformation, thresholding of coefficients, inverse transformation, and resampling to the original surface. On the other hand, the computation time for the Gaussian kernel smoothing increased with the FWHM. For example, the local optimal Gaussian filter of 2 mm FWHM required about 0.3 s while wider kernels of 10 and 14 mm took around 10 and 20 s, respectively. In spite of the obvious time differences between the two smoothing methods, the spherical wavelet approach seems to provide an excellent trade-off between computational time and image resolution when group comparisons are planned.

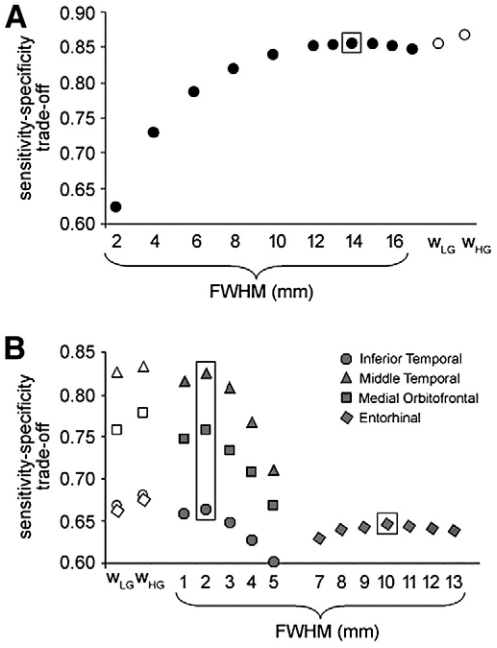

Fig. 2. Sensitivity–specificity trade-off for different kernel sizes and different wavelet transforms on equiangular grids of 1024^2 (low grid, LG) and 2048^2 (high grid, HG). A. Trade-off for the global-based analysis. Note that optimal values of trade-off were obtained for the Gaussian 14 mm FWHM (within a square) and for the wavelet transforms with an oscillation factor of 1 and dilation factors of 6 and 11 for the LG and HG, respectively. The number of threshold-finest levels was set to 3. B. Trade-off for the local-based analysis. The best trade-off was found for the Gaussian filter of 2 mm FWHM in all Brodmann's areas except in the entorhinal cortex, whose kernel width was set to 10 mm. In the case of the wavelet-based method, the best trade-off in the entorhinal cortex was obtained with dilation factors of 5 and 7 while in the remaining areas it decreased to 4 and 5 for LG and HG, respectively. The number of threshold-finest levels were set to 3 for entorhinal cortex, but it was reduced to 1 for the remaining regions.

Fig. 3 shows the cortical thickness maps of one experimental subject on the sphere (horizontal top panel) and the inflated cortical surface (horizontal bottom panel) in the original thickness map (left column) and after smoothing with the local optimal 10 mm Gaussian kernel (middle column) as well as the corresponding optimal wavelet filter on a grid of 2048^2 (right column) for the entorhinal cortex. These filters illustrate well the expected differences between the two smoothing methods. Indeed, note that the wavelet-

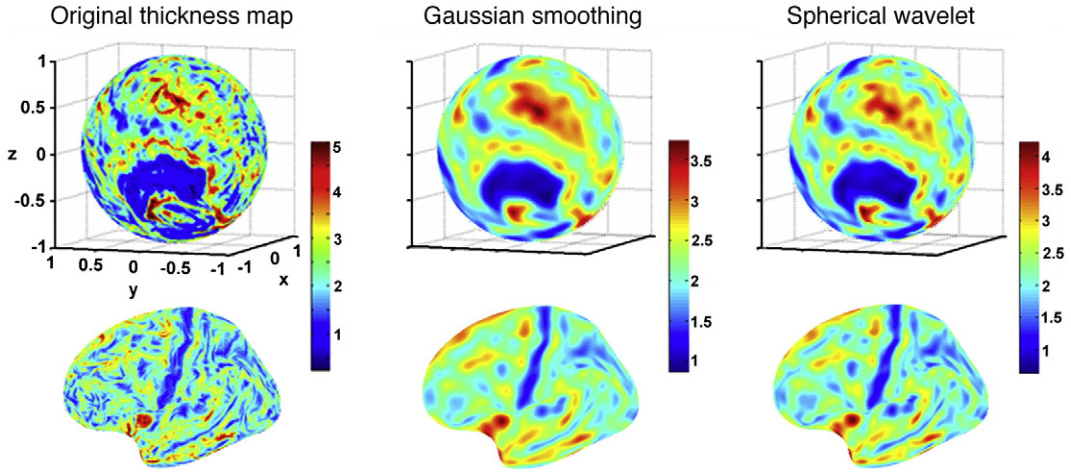

Fig. 3. Representation of the cortical thickness maps obtained from one control subject (female, 74 yr) before and after smoothing the original image (left column) with a Gaussian filter of 10 mm (middle column) and a wavelet filter with dilation factor of 7 (right column) on a grid of 2048^2. Both filters are the corresponding optimal settings for the entorhinal cortex. Spherical (upper panel) and inflated surface representations (bottom panel) of the cortical thickness map are displayed. Values of the colormap bars are expressed in mm.

based filter preserved the edges of the original signal better as compared to the Gaussian spatial filter. These properties will increase the reliability at detecting changes in cortical thickness in cross-sectional studies.

Intersubject variability

Estimation of sensitivity and specificity is heavily dependent on the degree of intersubject variability. The smoothing process not only reduces the noise from the raw thickness maps but also decreases the intersubject variability. The mean standard deviations computed on the cortical thickness at all cortical vertices across subjects before and after applying different filters are shown in Table 3 for both control and experimental groups. Changes in intersubject variability were analyzed in a two-way mixed ANOVA with the smoothing method (Gaussian and wavelet) as the within-subject factor and group (control *versus* experimental) as the between-subject factor. These analyses were performed for grids of 1024^2 and 2048^2, separately. Differences between smoothing methods were significant [$F(2,28)=52.82$; $p<10^{-5}$; $\varepsilon=.54$]. Pair-wise comparisons revealed that the smallest values of intersubject variability were provided by the Gaussian filter ($M=.353$, SE$=.033$) as compared with the 1024^2 ($M=.361$, SE$=.032$, $p<.005$) and 2048^2 ($M=.394$, SE$=.036$, $p<10^{-7}$) wavelet grids. There was no difference between the control and experimental group. The fact that wavelets often provided higher intersubject variability values discards intersubject variability as a possible explanation for any benefit of the adaptive wavelet filtering over the Gaussian smoothing.

Effects of whole-brain FDR thresholds on cortical thinning detection

Before introducing any synthetic change in cortical thickness, the two groups of subjects ($N=35$) were compared for this feature to ensure that no bias was accidentally introduced. As expected, no differences between groups were found, for neither Gaussian nor for wavelet-based smoothing. This conclusion was derived from the fact that the same values were obtained for the FDR threshold and the maxima significance on the thickness statistical parametric

Table 3
Mean of the standard deviations computed at the vertices across the control/experimental thickness maps before and after smoothing with the optimal Gaussian kernels and wavelets for global and local FDR thresholding

Threshold	Smoothing filter	Global	Inferior temporal	Medial temporal	Entorhinal	Medial orbitofrontal
	No filter before synthetic changes	.509/.497	.670/.656	.544/.548	.739/.718	.592/.571
	No filter after synthetic changes [a]	/.506	/.768	/.693	/.870	/.649
Global FDR thresholding						
	G-14 mm	.202/.193	.258/.226	.213/.175	.326/.322	.226/.193
	W-1-6 (1024^2)	.215/.205	.276/.245	.224/.190	.342/.339	.241/.207
	W-1-11 (2048^2)	.225/.215	.289/.259	.235/.204	.356/.361	.252/.218
Local FDR thresholding						
	G-2 mm		.580/.522	.475/.442	.380/.363 [b]	.506/.442
	W-1-4 (1024^2)		.580/.525	.474/.447	.371/.361 [b]	.506/.443
	W-1-5 (2048^2)		.617/.592	.504/.518	.433/.430 [b]	.542/.497

[a] Synthetic changes were only included in the experimental group.
[b] Gaussian FWHM of 10 mm, W-1-5 (1024^2), W-1-7 (2048^2).

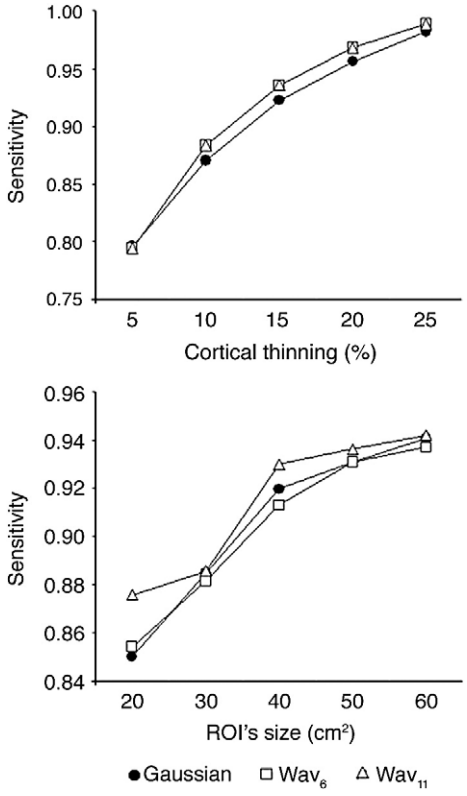

Fig. 4. Effects of global thresholding on sensitivity of cortical thickness analyses for different thinning percents (top panel) and different ROI sizes (bottom panel) after applying a Gaussian filter of 14 mm FWHM and wavelet transforms with dilation factors of 6 and 11 for equiangular grids of 1024^2 and 2048^2, respectively.

maps ($p=.0017$ for the Gaussian kernel of 14 mm, $p=.0016$ for the wavelet on a grid of 1024^2 and $p=.0013$ for the wavelet on a grid of 2048^2).

To determine if the wavelet approach was more efficient as compared to the Gaussian smoothing at correctly identifying changes in cortical thickness, the sensitivity yielded by the Gaussian filter and the two wavelet filters (grids of 1024^2 and 2048^2) was computed across 25 thickness statistical parametric maps (5 ROI sizes × 5 levels of thickness reduction). Although both the Gaussian and wavelet-based filters were highly accurate at detecting cortical thinning, the wavelet transform applied on the 2048^2 grid showed a slightly, but significantly higher sensitivity ($p<.003$) when compared with wavelets applied on 1024^2 grids and Gaussian smoothing. As shown in Fig. 4, all three filters increased their sensitivity as cortical thinning became more pronounced and as the ROI's size became larger.

Like sensitivity, the wavelet smoothing methods applied to different grid sizes were statistically more specific than the Gaussian smoothing ($p<10^{-24}$). In fact, the wavelet transform on the larger grid yielded 46% fewer false positives than the Gaussian filter. This difference was limited to 6% when the wavelet was applied on a grid of 1024^2. In our study, false positives not only included the statistical false positive vertices but also those generated in the smoothing process.

Results shown in Fig. 5 illustrate the decrease of specificity as the cortical thinning and ROI size increased. False positive vertices were found both inside and outside those regions artificially modified in the present study. We estimated the slopes of the lines that best fit the specificity values reported for each cortical thickness reduction and total modified area (resulting from adding the areas of the four cortical regions for each ROI size). In particular, specificity decreased at a higher rate for the Gaussian spatial procedure with the increase of cortical thinning. The difference between the two methods was statistically corroborated by computing the fitness for the values of the slopes again and considering the resulting second order slope as a measure of the specificity degradation acceleration (right inferior panel of Fig. 5).

The one-way ANOVA also revealed a significant effect of the smoothing on sensitivity–specificity trade-off [$F(2,48)=23.19$; $p<10^{-7}$]. The optimum trade-off was provided by the 2048^2 wavelet grid ($p<10^{-4}$), and as for sensitivity and specificity, its

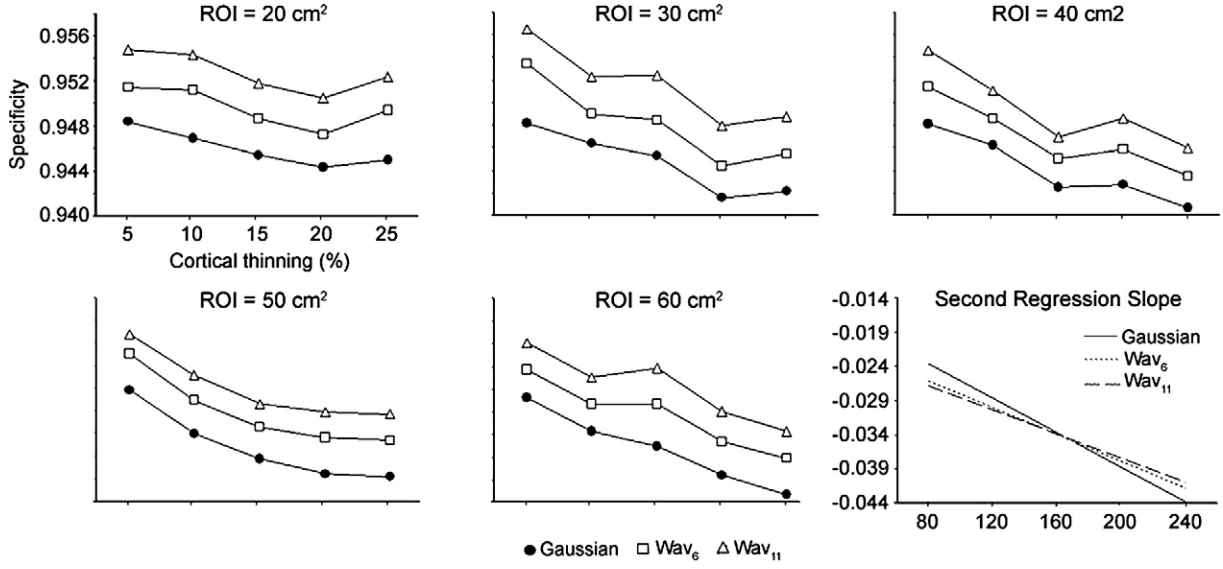

Fig. 5. Effects of thickness reduction on specificity for each ROI size after applying a Gaussian filter of 14 mm FWHM and wavelet transforms with dilation factors of order 6 and 11 for equiangular grids of 1024^2 and 2048^2, respectively. The right inferior panel shows the fitness of the second order slopes regression resulting from line fit of specificity computed for each ROI size within the four Brodmann's areas.

performance increased with the cortical thinning and size of the ROI.

The higher sensitivity and specificity of the wavelet smoothing method (for a grid of 2048^2) relative to the Gaussian spatial filter (14 mm FHWM) is also illustrated in Fig. 6, which shows the difference image after subtracting the statistical parametric maps yielded by the Gaussian (Fig. 6B) and wavelet filters (Fig. 6C) from the original image, when the ROI size was 20 cm^2 and cortical thickness decreased by 20% at the four cortical regions selected for this study. In this particular statistic parametric map, the two filters provided the same amount of true positives in all cortical regions (100% in inferior and medial temporal lobe, and 97% in medial orbitofrontal cortex) except in the entorhinal cortex, where the wavelet transform detected 16% more true modified vertices than the Gaussian filter. The wavelet reduced the amount of false positives detected from 8795 to 7777. Note that this reduction was particularly evident in entorhinal cortex and medial temporal lobe.

Effects of local FDR thresholds on cortical thinning detection

Progressive focal cortical atrophies appear in degenerative conditions characterizing different neurological and/or psychiatric disorders (Whitwell et al., 2007; Sailer et al., 2003; Didic et al., 1999). In these cases, changes in cortical thickness should be explored by applying local thresholding to thickness statistical parametric maps. Global thresholding procedures inherent in the FDR estimator do not consider cross-regional variations in the distribution of the uncorrected *p*-values. Regardless of whether a specific cortical region shows high or low intersubject variability and population differences, the same threshold value will be applied to all cortical regions. Consequently, global thresholding procedures might result in a high occurrence of false positives. Thus, if a cortical region with high intersubject and/or inter-population variability is used in determining the global threshold level, thinning in a region with low variability will be masked by the high global threshold level, and therefore will go undetected. Conversely, if a region with low variability is used for establishing the global threshold level, thinning free regions with high levels of intersubject and/or inter-population variability will produce a high rate of false positives. Therefore, local thresholding procedures are supposed to increase the smoothing process specificity when applied to cortical thickness maps. Indeed, differences between global and local FDR thresholds can be seen by comparing results shown in Figs. 6 and 7 for a ROI of 20 cm^2 and 20% of cortical thinning. In this particular case, the local FDR thresholding reduced the amount of false positives by 80% as compared with the global FDR. When local FDR thresholds were computed for each cortical region, the wavelet transform reduced, on the average, the amount of false positives by 10%. This reduction reached 24% in the inferior temporal lobe and 8.6% in the entorhinal cortex.

The wavelet-based smoothing method not only showed a better trade-off [$F(2,48)=53.27$; $p<10^{-9}$; $\varepsilon=.76$], but also an improvement in sensitivity [$F(2,48)=16.27$; $p<10^{-4}$; $\varepsilon=.67$] and specificity [$F(2,48)=37.4$; $p<10^{-6}$; $\varepsilon=.64$] as compared to the Gaussian spatial filter. Differences in the sensitivity–specificity trade-off varied depending on the cortical region as inferred from the significant interaction effect [$F(6,144)=2.92$; $p<.04$; $\varepsilon=.53$]. Specifically, the wavelet transform for the larger grid always yielded a better trade-off than the Gaussian filter. The higher specificity provided by the former was mainly responsible for this improvement. For example, the Gaussian smoothing detected 3%

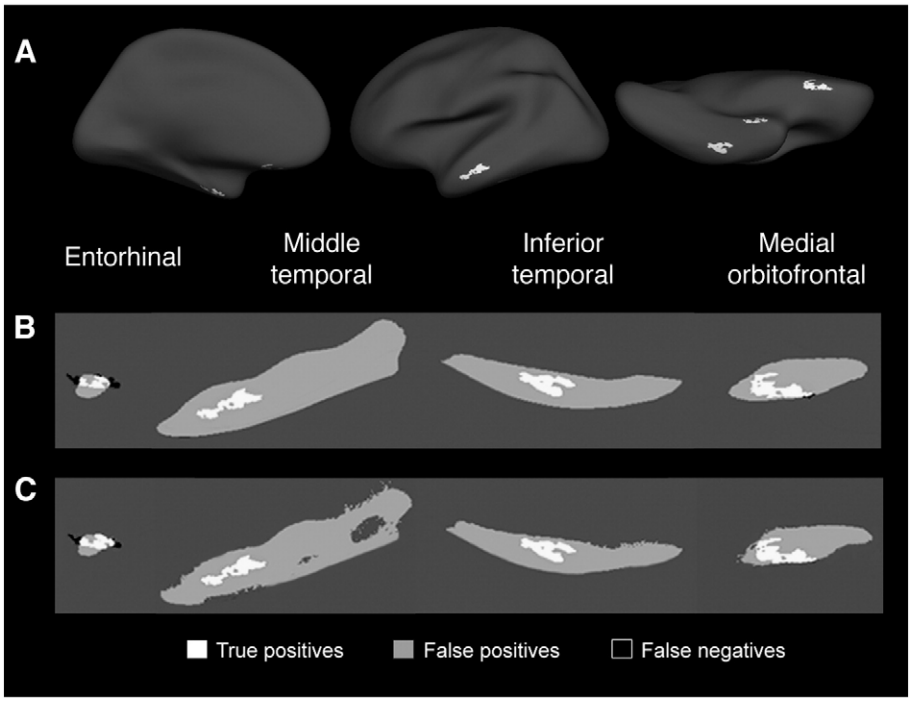

Fig. 6. True positives, false positives and true negatives yielded by the optimal filters within four Brodmann's areas after applying global FDR thresholding to thickness statistical parametric maps for a ROI size of 20 cm^2 and a 20% of simulated cortical thinning from the original signal. A. Simulated ROIs on the inflated surface. B. Results provided by the Gaussian spatial filter (FWHM = 14 mm). C. Results provided by the wavelet filter on an equiangular grid of 2048^2 (dilation factor = 11).

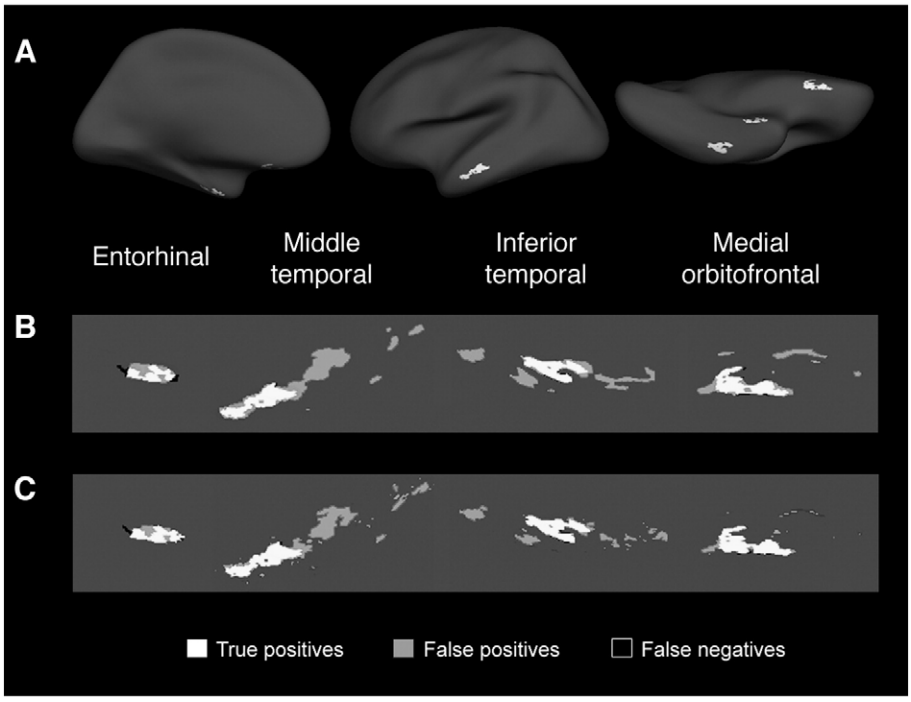

Fig. 7. True positives, false positives and true negatives yielded by the optimal filters within four Brodmann's areas after applying local FDR thresholding to thickness statistical parametric maps for a ROI size of 20 cm^2 and a 20% of simulated cortical thinning from the original signal. A. Simulated ROIs on the inflated surface. B. Results provided by the Gaussian spatial filter. The width of the kernel was set to 2 mm for all cortical regions except for entorhinal cortex which was set to 10 mm. C. Results provided by the wavelet filter on an equiangular grid of 2048^2 with dilation factors of order 7 for entorhinal cortex and order 5 for the remaining cortical regions.

less true positives and 24% more false positives in the inferior temporal lobe than the wavelet-based method. When the wavelet transform was applied on grids of 1024^2, the better sensitivity–specificity trade-off was restricted to the inferior area of the temporal lobe ($p<.03$) and the entorhinal cortex ($p<.001$), also due to its higher specificity ($p<10^{-14}$ and $p<.009$, respectively). These results are illustrated in Fig. 8.

Power analysis

We conducted power calculations in order to determine how many subjects are needed to detect global and local changes in cortical thickness when wavelet-based smoothing is applied. The sample size was estimated at a significance level of 0.05 (two-sided), with a statistical power of 0.9, and for a different percent of thickness reduction (effect size). Only sample size estimated results for a ROI size of 60 cm^2 are presented because results for the remaining ROI sizes were similar. Table 4 shows sample size estimates based on the estimated thickness measurement variability (standard deviation of measurement error).

As expected, the number of subjects per group necessary to detect global and local changes decreased as the cortical thinning increased. It is worth noting that changes affecting the entorhinal cortex demanded a relatively higher number of subjects to detect cortical atrophy as compared to the remaining cortical regions. Likewise, detection of cortical thinning in the whole cortex required quite a high number of subjects, a minimum of threefold more subjects than detection of local changes. Thus, caution is

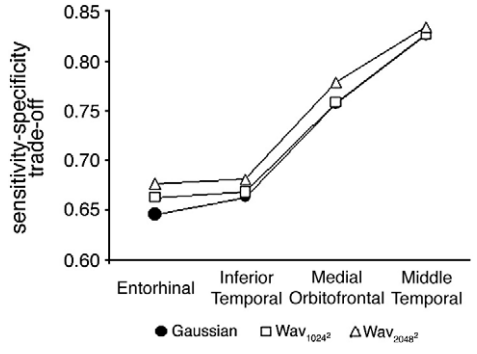

Fig. 8. Effects of local thresholding on the sensitivity–specificity trade-off in the four Brodmann's areas after applying optimal Gaussian and wavelet filters on equiangular grids of 1024^2 and 2048^2.

Table 4
Calculation of the sample sizes (subjects per group) required to detect (significance level at 0.05, two-sided, statistical power of 0.9) global and local thickness difference effects under various conditions of thickness reduction when using optimal wavelet smoothing

Thinning	STD	Percent of cortical thickness reduction				
		5%	10%	15%	20%	25%
Global	0.083	160	152	146	128	124
Inferior temporal	0.183	16	16	16	14	14
Medial temporal	0.154	16	16	14	12	12
Entorhinal	0.310	44	28	24	20	18
Medial orbitofrontal	0.169	20	18	16	16	16

required when interpreting mean global cortical thinning if the sample size is not large enough.

Discussion

The present study compares the sensitivity and specificity of two different smoothing methods to detect synthetic changes in human cortical thickness. Wavelet-based methods revealed a better sensitivity–specificity trade-off when compared to Gaussian smoothing in both the whole neocortex and cortical region-based statistical analyses, which was mainly due to the higher specificity obtained with the wavelet approach. All together, these results suggest that spherical wavelets represent a reliable alternative to Gaussian spatial filtering at detecting changes in cortical thickness in cross-sectional studies.

Results revealed that the wavelet-based method was more accurate at identifying changes in cortical thickness than Gaussian smoothing. Thus, spherical wavelets were more sensitive (more true positive results) and specific (less probability of false positive results) at detecting small cortical atrophies than the traditional approach based on spatial Gaussian filters. Among the wavelet methods evaluated, the one with a larger equiangular grid (2048^2) always improved the trade-off between sensitivity and specificity. This was possible because the increase in size of equiangular grid provided a larger bandwidth to represent the cortical surface variations which, in turn, lead to more precise spherical harmonic transform of the data (Wiaux et al., 2007). Interestingly, the enhanced performance of the wavelet filter relative to Gaussian smoothing was especially remarkable for the ROI size of 20 cm^2, even for cortical thickness reductions as small as 5% (M=0.46 mm), which might be of clinical interest in the early diagnosis and follow-up of neurodegenerative disorders characterized by progressive focal cortical atrophies (Whitwell et al., 2007; Rosas et al., 2005; Sailer et al., 2003; Didic et al., 1999).

Differences in accurate detection between the adaptive wavelet filtering and the Gaussian method increased in the local-based statistical analyses, mainly due to changes in specificity. It is noteworthy to mention that the higher specificity of the wavelet over the Gaussian smoothing cannot be attributed to a lack of sensitivity of the former because the wavelet procedure always produced more true positives. Changes in intersubject variability can also be ruled out as a possible explanation for the better sensitivity and specificity of the wavelet-based methods over the traditional Gaussian smoothing. In fact, the mean standard deviations either were similar for both procedures or were larger for the wavelet method. Alternatively, the smaller number of false positives detected by the wavelet filter could be due to the less smoothing effect introduced in the statistic parametric maps. In agreement with this idea, Wink and Roerdink (2004) found that the less smoothing wavelet-based methods applied to functional MRI data generated less false positives than Gaussian smoothing or wavelet-based methods with a larger smoothing effect.

In the current study, FDR was used to correct for multiple comparisons. It is known that FDR control is more advantageous than family-wise error control methods (e.g., Gaussian's random field theory), especially when the percentage of vertices affected by change is high relative to the whole surface. In such cases, sensitivity is kept quite high while the number of false positives is kept relatively low in comparison to the overall surface. Accordingly, we found that the trade-off between sensitivity and specificity increased with the ROI size and cortical thinning regardless of the smoothing procedure. Therefore, FDR is limited at detecting focal changes because it uses the amount of signal contained in the whole surface to set its threshold. To overcome this constraint, regional FDR control has recently been proposed as improving the power of the analysis (Langers et al., 2007). Alternatively, other approaches for correcting multiple comparisons could be used (Hagler et al., 2006). For example, an accurate approach would be to perform simulations under the null hypothesis to determine how often the value of a statistic from the 'true' analysis is exceeded. This frequency is then interpreted as a corrected p-value. This approach would considerably increase both computational demands and calculation time, which is especially important in our study, where a large number of thickness statistical parametric maps were tested.

Interestingly, wavelets were especially accurate at identifying thickness reductions within the inferior temporal lobe, one of the cortical structures whose pattern of thinning seems to differentiate between Alzheimer's disease and frontotemporal dementia (Du et al., 2007). Also, a significant thinning of inferior temporal gyrus has been reported to distinguish between healthy elderly and mild cognitive impairment, this gyrus being the region with the highest percent of atrophy when mild cognitive impairment and Alzheimer's disease populations were compared (Singh et al., 2006). Furthermore, wavelets provided a better sensitivity–specificity trade-off than traditional Gaussian smoothing at detecting cortical thinning within the entorhinal cortex. The volume of this structure has been reported to differentiate subjects with memory difficulty but not dementia from those destined to develop dementia with 84% accuracy (Killiany et al., 2002).

Considerable efforts have been made in the last decade to quantify changes in shape descriptors of different human brain structures by using distinct computational neuroanatomy approaches (Jang et al., 2006; Chung et al., 2003; Thompson et al., 2001, 2004; Fischl and Dale, 2000; Van Essen et al., 1998). Most of these techniques smooth the original cortical surfaces with Gaussian spatial filters in order to decrease the high-frequency noise and enhance the robustness of the parametric statistic tests at extracting shape features based on group comparisons. The main disadvantage of this pre-processing step is its reduced ability to localize focal changes in complex surfaces (e.g., neocortex) because it blurs the boundaries of the anatomical changes. The suppression of apparently undersized details in brain images has motivated the search for new methods able to preserve the main features of the original images for group comparisons. Within this framework, previous fMRI studies have already pointed out the wavelet approach as an excellent alternative to the Gaussian smoothing (Van de Ville et al., 2006, 2007; Wink and Roerdink, 2004). Nevertheless, those methods are 3D volume-based analyses and, to our knowledge, no prior study has compared surface-based wavelets and Gaussian smoothing on brain images. Surface-based methods take into account the geodesic surface and therefore can provide more accurate results than the volume-based ones (Thompson et al., 2004).

There have been previous attempts to smooth shape descriptors of human cerebral cortex using heat kernel smoothing on the unit sphere, and spherical harmonics for data modeling (Chung, 2006). This approach was later improved by weighting the spherical harmonics (Chung et al., 2006). The weighted spherical harmonic representation is the finite least square approximation to the solution of the isotropic heat diffusion on the unit sphere. This approach provides a better estimator of the local and detailed

features of the signal as compared to the classical spherical harmonics. However, it is not as adaptive as the wavelet shrinkage denoising. The wavelet-based method has been theoretically proven to be nearly optimal regarding the spatial adaptation when global and local smoothness are unknown (Donoho, 1995; Donoho and Johnstone, 1994). To the best of our knowledge, no alternative estimation procedure performs better without knowing *a priori* the smoothness class of the signal. Even though our wavelet smoothing approach does not use spherical orthonormal basis (which is crucial in the wavelet shrinkage denoising mathematical framework) but just as an overcomplete representation, it could enhance adaptation. Shrinkage is also possible with redundant representations if the smooth underlying signal has a sparse representation with respect to the used frames. Likewise, wavelet filters do not require assumptions about the nature of the signal and they allow discontinuities and spatial variation (Donoho, 1995; Donoho and Johnstone, 1994).

Recent studies have confirmed the above-mentioned advantages of spherical wavelets in shape analysis of different brain structures. Thus, Yu et al. (2007) studied the pattern of shape variations in cortical features within normal population by applying discrete biorthogonal spherical wavelet transformation to cortical surfaces and separated principal component analysis to each scale of correlated spherical wavelet coefficients, in comparison with a decomposition of cortical surface using a spherical harmonic basis function approach. These authors found that the spherical wavelet transformation was able to detect locations of specific shape variations in non-demented elderly people more accurately, as well as tracking the development of cortical surface folding pattern in newborns. Determining shape variations at multiple scales using spherical wavelet transformation can also improve the segmentation of subcortical structures. Thus, Nain et al. (2007) applied the same spherical wavelet functions as Yu et al. (2007) to the automatic segmentation of human caudate nucleus and hippocampus, two regions of interest in the study of schizophrenia. This wavelet shape-based analysis approach significantly improved the approximation of shapes relative to the point distribution model, which tends to over smooth data. Additionally, spherical wavelets performed better than the active shape model algorithm at capturing finer shape details during the automatic segmentation process of both brain structures.

One potential field of application of spherical wavelet-based cortical thickness analysis would be the early diagnosis of neurodegenerative conditions. This procedure might be useful at establishing a link between preclinical symptoms and local anatomical changes in neurological disorders with different etiology. In support of this proposal, there is increasing evidence that focal atrophies are associated with the onset and/or preclinical stages of different neurodegenerative conditions. For instance, the initial clinical symptoms of multiple sclerosis are correlated with cortical grey matter loss in affected regions, which seems to be independent of white matter pathology (Calabrese et al., 2007). It has also been found that focal thinning of grey matter affects different cortical regions during the course of the disease (Sailer et al., 2003). Further evidence has shown a strong correlation between focal cortical degeneration and cognitive performance impairment during the motor preclinical stages of Huntington disease, calling attention to the critical role of cortical damage in the pathophysiology and clinical expression of the disease (Rosas et al., 2005). Finally, different patterns of cortical atrophy underlie distinct subtypes of mild cognitive impairment, hallmark of some prevalent neurodegenerative diseases (Seo et al., 2007; Bell-McGinty et al., 2005). All together, these findings suggest that determining the spatiotemporal course of subtle thickness variations in both healthy aging and preclinical conditions will provide important insight into better tracking of the neuronal loss route during normal aging and to find early markers of cortical lesions in prevalent neurodegenerative diseases.

Acknowledgments

The authors wish to thank Dr. Randy Buckner (Harvard University), the Neuroinformatics Research Group (Washington University School of Medicine), and the Biomedical Informatics Research Network for making available the OASIS MRI data set used in the present study. Also we thank Dr. Pierre Vandergheynst (Signal Processing Institute, Ecole Polytechnique Fédérale de Lausanne, Switzerland) and Dr. Laurent Jacques (Institut de Physique Théorique, Université Catholique de Louvain, Belgium) for providing the Matlab code of the pyramidal wavelet decomposition and useful comments on spherical wavelets. This research was supported by grants from the European Union (FP6-2005-NEST-Path 043309), Spanish Ministry of Education and Science (SAF2005-00398), Regional Ministry of Innovation, Science and Enterprise, Junta de Andalucia (CTS-229), and the CIBERNED (Network for Biomedical Research in Neurodegenerative Diseases, Spanish Ministry of Health).

References

Ad-Dab'bagh, Y., Singh, V., Robbins, S., Lerch, J., Lyttelton, O., Fombonne, E., Evans, A.C., 2005. Native space cortical thickness measurement and the absence of correlation to cerebral volume. Proceedings of the 11th Annual Meeting of the Organization for Human Brain Mapping. Toronto.

Amunts, K., Schleicher, A., Zilles, K., 2002. Architectonic mapping of the human cerebral cortex. In: Schüz, A., Miller, R. (Eds.), Cortical Areas: Unity and Diversity. Taylor & Francis, London, pp. 29–52.

Antoine, J.P., Vandergheynst, P., 1999. Wavelets on the 2-Sphere: a Group Theoretical Approach. Appl. Comput. Harmon. Anal. 7, 262–291.

Antoine, J.P., Demanet, L., Jacques, L., Vandergheynst, P., 2001. Wavelets on the sphere: implementations and approximations. Appl. Comput. Harmon. Anal. 13, 177–200.

Antoine, J.P., Demanet, L., Hochedez, J.F., Jacques, L., Terrier, R., Verwichte, E., 2002. Application of the 2-D wavelet transform to astrophysical images. Phys. Mag. 24, 93–116.

Bell-McGinty, S., Lopez, O.L., Meltzer, C.C., Scanlon, J.M., Whyte, E.M., Dekosky, S.T., Becker, J.T., 2005. Differential cortical atrophy in subgroups of mild cognitive impairment. Arch. Neurol. 62, 1393–1397.

Biega, T.J., Lonser, R.R., Butman, J.A., 2006. Differential cortical thickness across the central sulcus: a method for identifying the central sulcus in the presence of mass effect and vasogenic edema. Am. J. Neuroradiol. 27, 1450–1453.

Bullmore, E., Fadili, J., Breakspear, M., Salvador, R., Suckling, J., Brammer, M.J., 2003. Wavelets and statistical analysis of functional magnetic resonance images of the human brain. Stat. Methods Med. Res. 12, 375–399.

Butman, J.A., Floeter, M.K., 2007. Decreased thickness of primary motor cortex in primary lateral sclerosis. Am. J. Neuroradiol. 28, 87–91.

Calabrese, M., Atzori, M., Bernardi, V., Morra, A., Romualdi, C., Rinaldi, L., McAuliffe, M.J., Barachino, L., Perini, P., Fischl, B., Battistin, L., Gallo, P., 2007. Cortical atrophy is relevant in multiple sclerosis at clinical onset. J. Neurol. 254, 1212–1220.

Cesar, R.M., Costa, L.F., 1998. Neural cell classification by wavelets and multiscale curvature. Biol. Cybern. 79, 347–360.

Charil, A., Dagher, A., Lerch, J.P., Zijdenbos, A.P., Worsley, K.J., Evans, A.C., 2007. Focal cortical atrophy in multiple sclerosis: relation to lesion load and disability. NeuroImage 34, 509–517.

Chung, M.K., 2006. Heat kernel smoothing on unit sphere. IEEE International Symposium on Biomedical Imaging. Arlington (Virginia).

Chung, M.K., Worsley, K.J., Robbins, S., Paus, P., Taylor, J., Giedd, J.N., Rapoport, J.L., Evans, A.C., 2003. Deformation-based surface morphometry applied to gray matter deformation. NeuroImage 18, 198–213.

Chung, M.K., Robbins, S.M., Dalton, K.M., Davidson, R.J., Alexander, A.L., Evans, A.C., 2005. Cortical thickness analysis in autism with heat kernel smoothing. NeuroImage 25, 1256–1265.

Chung, M.K., Robbins, S., Dalton, K.M., Wang, S., Evans, A.C., Davidson, R.J., 2006. Tensor-based cortical surface morphometry via weighted spherical harmonic representation. IEEE Computer Society Workshop on Mathematical Methods in Biomedical Image Analysis (MMBIA). New York.

Dale, A.M., Fischl, B., Sereno, M.I., 1999. Cortical surface-based analysis. I. Segmentation and surface reconstruction. NeuroImage 9, 179–194.

Daubechies, I., Teschke, G., 2005. Variational image restoration by means of wavelets: simultaneous decomposition, deblurring and denoising. Appl. Comput. Harmon. Anal., 19, 1–16.

Daubechies, I., 1992. Ten Lectures on Wavelets. Society for Industrial and Applied Mathematics, Philadelphia.

Desikan, R.S., Segonne, F., Fischl, B., Quinn, B.T., Dickerson, B.C., Blacker, D., Buckner, R.L., Dale, A.M., Maguire, R.P., Hyman, B.T., Albert, M.S., Killiany, R.J., 2006. An automated labeling system for subdividing the human cerebral cortex on MRI scans into gyral based regions of interest. NeuroImage 31, 968–980.

Didic, M., Felician, O., Ceccaldi, M., Poncet, M., 1999. Progressive focal cortical atrophies. Rev. Neurol. (Paris) 155, 73–82.

Donoho, D.L., 1995. De-noising by soft-thresholding. IEEE, Trans. on Inf. Theory 41, 613–627.

Donoho, D.L., Johnstone, I.M., 1994. Ideal spatial adaptation by wavelet shrinkage. Biometrika 81, 425–455.

Driscoll, J.R., Healy, D.M., 1994. Computing Fourier transforms and convolutions on the 2-sphere. Adv. Appl. Math. 15, 202–250.

Du, A.T., Schuff, N., Kramer, J.H., Rosen, H.J., Gorno-Tempini, M.L., Rankin, K., Miller, B.L., Weiner, M.W., 2007. Different regional patterns of cortical thinning in Alzheimer's disease and frontotemporal dementia. Brain 130, 1159–1166.

Duncan, J.S., Papademetris, X., Yang, J., Jackowski, M., Zeng, X., Staib, L.H., 2004. Geometric strategies for neuroanatomic analysis from MRI. NeuroImage 23, 34–45.

Fadili, M.J., Bullmore, E.T., 2004. A comparative evaluation of wavelet-based methods for hypothesis testing of brain activation maps. NeuroImage 23, 1112–1128.

Fischl, B., Dale, A.M., 2000. Measuring the thickness of the human cerebral cortex from magnetic resonance images. Proc. Natl. Acad. Sci. U. S. A. 97, 11050–11055.

Fischl, B., Sereno, M.I., Dale, A.M., 1999a. Cortical surface-based analysis: II. Inflation, flattening, and a surface-based coordinate system. NeuroImage 9, 195–207.

Fischl, B., Sereno, M.I., Tootell, R.B.H., Dale, A.M., 1999b. High-resolution intersubject averaging and a coordinate system for the cortical surface. Hum. Brain Mapp. 8, 272–284.

Fischl, B., Liu, A., Dale, A.M., 2001. Automated manifold surgery: constructing geometrically accurate and topologically correct models of the human cerebral cortex. IEEE Trans. Med. Imag. 20, 70–80.

Fjell, A.M., Walhovd, K.B., Reinvang, I., Lundervold, A., Salat, D., Quinn, B.T., Fischl, B., Dale, A.M., 2006. Selective increase of cortical thickness in high-performing elderly—structural indices of optimal cognitive aging. NeuroImage 29, 984–994.

Genovese, C.R., Lazar, N.A., Nichols, T., 2002. Thresholding of statistical maps in functional neuroimaging using the false discovery rate. NeuroImage 15, 870–878.

Good, J., Ashburner, C.D., Frackowiak, R.S., 2001. Computational neuroanatomy: new perspectives for neuroradiology. Rev. Neurol. (Paris) 157, 797–806.

Hagler, D.J., Saygin, A.P., Sereno, M.I., 2006. Smoothing and cluster thresholding for cortical surface-based group analysis of fMRI data. NeuroImage 33, 1093–1103.

Han, X., Jovicich, J., Salat, D., Van der Kouwe, A., Quinn, B., Czanner, S., Busa, E., Pacheco, J., Albert, M., Killiany, R., Maguire, P., Rosas, D., Makris, N., Dale, A., Dickerson, B., Fischl, B., 2006. Reliability of MRI-derived measurements of human cerebral cortical thickness: the effects of field strength, scanner upgrade and manufacturer. NeuroImage 32, 180–194.

Healy, D., Rockmore, D., Kostelec, P., Moore, S., 2003. Ffts for the 2-sphere — improvements and variations. J. Fourier Anal. Appl. 9, 341–385.

Jang, D.P., Kim, J.J., Chung, T.S., An, S.K., Jung, Y.C., Lee, J.K., Lee, J.M., Kim, I.Y., Kim, S.I., 2006. Shape deformation of the insula in schizophrenia. NeuroImage 32, 220–227.

Kavitha, A., Ramakrishnan, S., 2005. Analysis on the erythrocyte shape changes using wavelet transforms. Clin. Hemorheol. Microcirc. 33, 327–335.

Killiany, R.J., Hyman, B.T., Gomez-Isla, T., Moss, M.B., Kikinis, R., Jolesz, F., Tanzi, R., Jones, K., Albert, M.S., 2002. MRI measures of entorhinal cortex vs hippocampus in preclinical AD. Neurology 58, 1188–1196.

Kuperberg, G.R., Broome, M.R., McGuire, P.K., David, A.S., Eddy, M., Ozawa, F., Goff, D., West, W.C., Williams, S.C., Van der Kouwe, A.J., Salat, D.H., Dale, A.M., Fischl, B., 2003. Regionally localized thinning of the cerebral cortex in schizophrenia. Arch. Gen. Psychiatry 60, 878–888.

Laine, 2000. Wavelets in temporal and spatial processing of biomedical images. Annu. Rev. Biomed. Eng. 2, 511–550.

Langers, D.R.M., Jansen, J.F.A., Backes, W.H., 2007. Enhanced signal detection in neuroimaging by means of regional control of the global false discovery rate. NeuroImage, 38, 43–56.

Lerch, J.P., Evans, A.C., 2005. Cortical thickness analysis examined through power analysis and a population simulation. NeuroImage 24, 163–173.

Lerch, J.P., Pruessner, J.C., Zijdenbos, A., Hampel, H., Teipel, S.J., Evans, A.C., 2005. Focal decline of cortical thickness in Alzheimer's disease identified by computational neuroanatomy. Cereb. Cortex 15, 995–1001.

Lyoo, I.K., Sung, Y.H., Dager, S.R., Friedman, S.D., Lee, J.Y., Kim, S.J., Kim, N., Dunner, D.L., Renshaw, P.F., 2006. Regional cerebral cortical thinning in bipolar disorder. Bipolar Disord. 8, 65–74.

Makris, N., Biederman, J., Valera, E.M., Bush, G., Kaiser, J., Kennedy, D.N., Caviness, V.S., Faraone, S.V., Seidman, L.J., 2007. Cortical thinning of the attention and executive function networks in adults with attention-deficit/hyperactivity disorder. Cereb. Cortex 17, 1364–1375.

Mallat, S., 1999. Wavelet Tour of Signal Processing. Academic Press, New York.

Mallat, S., 1989. A theory for multiresolution signal decomposition: the wavelet decomposition. IEEE Trans. Pattern Anal. Mach. Intell. 7, 674–693.

McEwen, J.D., Hobson, M.P., Mortlock, D.J., Lasenby, A.N., 2007. Fast directional continuous spherical wavelet transform algorithms. IEEE Trans. Signal. Proc. 55, 520–529.

Nain, D., Haker, S., Bobick, A., Tannenbaum, A., 2007. Multiscale 3D shape representation and segmentation using spherical wavelets. IEEE Trans. Med. Imaging 26, 598–618.

Nenadic, Z., Burdick, J.W., 2005. Spike detection using the continuous wavelet transform. IEEE Trans. Biomed. Eng. 52, 74–87.

Petersson, K.M., Nichols, T.E., Poline, J.B., Holmes, A.P., 1999. Statistical limitations in functional neuroimaging. II. Signal detection and statistical inference. Philos. Trans. R. Soc. Lond., B 354, 1261–1281.

Preul, C., Lohmann, G., Hund-Georgiadis, M., Guthke, T., Von Cramon, D.Y., 2005. Morphometry demonstrates loss of cortical thickness in cerebral microangiopathy. J. Neurol. 252, 441–447.

Rakic, P., 1988. Specification of cerebral cortical areas. Science 241, 170–176.

Rosas, H.D., Hevelone, N.D., Zaleta, A.K., Greve, D.N., Salat, D.H., Fischl, B., 2005. Regional cortical thinning in preclinical Huntington disease and its relationship to cognition. Neurology 65, 745–747.

Sailer, M., Fischl, B., Salat, D., Tempelmann, C., Schonfeld, M.A., Busa, E., Bodammer, N., Heinze, H.J., Dale, A., 2003. Focal thinning of the cerebral cortex in multiple sclerosis. Brain 126, 1734–1744.

Seo, S.W., Im, K., Lee, J.M., Kim, Y.H., Kim, S.T., Kim, S.Y., Yang, D.W., Kim, S.I., Cho, Y.S., Na, D.L., 2007. Cortical thickness in single- *versus* multiple-domain amnestic mild cognitive impairment. NeuroImage 36, 289–297.

Shaw, P., Lerch, J., Greenstein, D., Sharp, W., Clasen, L., Evans, A., Giedd, J., Castellanos, F.X., Rapoport, J., 2006. Longitudinal mapping of cortical thickness and clinical outcome in children and adolescents with attention-deficit/hyperactivity disorder. Arch. Gen. Psychiatry 63, 540–549.

Singh, V., Chertkow, H., Lerch, J.P., Evans, A.C., Dorr, A.E., Kabani, N.J., 2006. Spatial patterns of cortical thinning in mild cognitive impairment and Alzheimer's disease. Brain 129, 2885–2893.

Thompson, P.M., Mega, M.S., Woods, R.P., Zoumalan, C.I., Lindshield, C.J., Blanton, R.E., Moussai, J., Holmes, C.J., Cummings, J.L., Toga, A.W., 2001. Cortical change in Alzheimer's disease detected with a disease-specific population-based brain atlas. Cereb. Cortex 11, 1–16.

Thompson, P.M., Hayashi, K.M., Sowell, E.R., Gogtay, N., Giedd, J.N., Rapoport, J.L., De Zubicaray, G.I., Janke, A.L., Rose, S.E., Semple, J., Doddrell, D.M., Wang, Y., Van Erp, T.G.M., Cannon, T.D., Toga, A.W., 2004. Mapping cortical change in Alzheimer's disease, brain development, and schizophrenia. NeuroImage 23, S2–S18.

Thompson, P.M., Hayashi, K.M., Dutton, R.A., Chiang, M.C., Leow, A.D., Sowell, E.R., De Zubicaray, G., Becker, J.T., Lopez, O.L., Aizenstein, H.J., Toga, A.W., 2007. Tracking Alzheimer's disease. Ann. N. Y. Acad. Sci. 1097, 183–214.

Uhlhaas, P.J., Singer, W., 2006. Neural synchrony in brain disorders: relevance for cognitive dysfunctions and pathophysiology. Neuron 52, 155–168.

Van de Ville, D., Seghier, M.L., Lazeyras, F., Blu, T., Unser, M., 2007. WSPM: Wavelet-based statistical parametric mapping. NeuroImage 37, 1205–1217.

Van de Ville, D., Blu, T., Unser, M., 2006. Surfing the brain. An overview of wavelet-based techniques for fMRI data analysis. IEEE Eng. Med. Biol. Mag. 25, 65–78.

Van Essen, H., Drury, S., Miller, J., Miller, M., 1998. Functional and structural mapping of human cerebral cortex: solution are in the surfaces. Proc. Natl. Acad. Sci. U. S. A. 95, 788–795.

Watson, D.F., 1992. Contouring: A Guide to the Analysis and Display of Spatial Data. Pergamon (Elsevier Science, Inc.), Tarrytown, NY.

Whitwell, J.L., Weigand, S.D., Shiung, M.M., Boeve, B.F., Ferman, T.J., Smith, G.E., Knopman, D.S., Petersen, R.C., Benarroch, E.E., Josephs, K.A., Jack, C.R., 2007. Focal atrophy in dementia with Lewy bodies on MRI: a distinct pattern from Alzheimer's disease. Brain 130, 708–719.

Wiaux, Y., Jacques, L., Vandergheynst, P., 2005. Corresponding principle between spherical and Euclidean wavelets. Astrophysics 632, 15–28.

Wiaux, Y., McEwen, J.D., Vandergheynst, P., Blanc, O., 2007. Exact reconstruction with directional wavelets on the sphere. Mon. Not. R. Astron. Soc. 000, 1–18.

Wink, A.M., Roerdink, J.B.T.M., 2004. Denoising functional MR images: a comparison of wavelet denoising and Gaussian smoothing. IEEE Trans. Med. Imaging 23, 374–387.

Yeo, B.T.T., Ou, W., Golland, P., 2006. On the construction of invertible filter bank on the 2-sphere. Technical Report, http://people.csail.mit.edu/ythomas/IFB2006.pdf.

Yu, P., Grant, P.E., Qi, Y., Han, X., Segonne, F., Pienaar, R., Busa, E., Pacheco, J., Makris, N., Buckner, R.L., Golland, P., Fischl, B., 2007. Cortical surface shape analysis based on spherical wavelets. IEEE Trans. Med. Imaging 26, 582–597.